


Magnon-Fluxon Interaction in Coupled Superconductor/Ferromagnet Hybrid Periodic Structures

B. Niedzielski,¹ C.L. Jia², and J. Berakdar^{1,*}

¹*Institut für Physik, Martin-Luther Universität Halle-Wittenberg, Halle/Saale 06099, Germany*

²*Key Laboratory for Magnetism and Magnetic Materials of the Ministry of Education and Lanzhou Center for Theoretical Physics, Lanzhou University, Lanzhou 73000, China*

 (Received 8 September 2022; revised 7 December 2022; accepted 6 February 2023; published 28 February 2023)

We study the magnon propagation in a micrometer-size ferromagnetic waveguide affected by the proximity to a superconductor that hosts a vortex formation. By solving the time-dependent Ginzburg-Landau equations of superconductivity, we obtain the equilibrium state of the vortex configuration and the associated stray fields that act on the magnetic dynamics. Spin wave dynamics in the presence of the superconductors are inferred from the Landau-Lifschitz equation. For a quantitative comparison, the simulations are performed under the experimental conditions as reported by Dobrovolskiy *et al.* (Nature Physics, **15**, 477 (2019)). We found that the presence of the vortex lattice leads to the formation of a Bloch-like band structure in the magnon spectrum. The width and the number of allowed bands are found to depend mainly on the in-plane component of the vortex field along the waveguide. A shift to lower energies of the lowest-order-allowed bands occurs due to the confinement of the magnonic modes above the locations of the superconductor vortices. We also studied the role of the films thickness. At least two GHz-frequency backward-volume magnetostatic spin waves modes are observed at the top and bottom surfaces (in addition to these magnetostatic surface modes, the vertical confinement can also give rise to longer-wavelength and low-frequency perpendicular standing spin waves). Effects of the vortex fields are found to depend strongly on the type of the magnon modes. It is found that the effect of the superconducting vortices of the spin waves can be emulated well by the stray fields of air-separated magnetic nanocubes of appropriate dimensions.

DOI: [10.1103/PhysRevApplied.19.024073](https://doi.org/10.1103/PhysRevApplied.19.024073)

I. INTRODUCTION

Studying the inter-relation between magnetism and superconductivity is fundamentally important for the understanding of both phenomena and their use in technology [1–4]. For instance, minute magnetic or stray fields can be sensed by the dynamics they drive in a superconducting ring. While some (type I) superconductors (SCs) resist the penetration of magnetic fields, others (type II SCs) may funnel it through the cores of SC vortices. Superconductivity and magnetism may coexist in some materials [4]. In general, however, the intrinsic coupling between SCs and magnetism is weak but can be increased substantially by proximity effects. Examples are multilayers and nanostructures comprising SCs adjacent to magnetic materials [5]. A SC influenced by the exchange field of a ferromagnet (FM) may develop an interfacial magnetic correlation whose sign and amplitude are material and interface specific (such as layer thickness and strength of impurity scattering) [6–10]. Experiments utilizing ferromagnetic resonance,

neutron scattering, muon scattering, and other methods provided evidence of the interfacial coupling between SC and magnetic correlations [10–17] which is manifested, for instance, by the presence of a magnetic moment in the SC arising upon a strong hybridization and orbital reconstruction (chemical bonds) among the atoms in the vicinity (few nanometers) of the interface [18].

If the SC and FM are well separated (e.g., by a spacer layer inhibiting direct hybridization), the SC and FM correlation may still affect each other, for example via the stray fields of the FM acting on the SC or by the vector potential of SC vortices in a type II SC that influences the FM [19–32]. From a technological point of view, FM/SC layers may be useful. For example, the transport properties of clean SC islands are affected by the dynamic of vortices which are coupled in SC/FM to the magnetic dynamics so allowing a local magnetic control of the SC. In turn, as discussed here, individual, multiple, or a lattice of vortices have a strong influence on magnetic excitations. In the following, we study mostly static vortices acting on the magnonic dynamics in the FM. As shown in the Appendix, however, the time-dependent magnetic fields involved in

*jamal.berakdar@physik.uni-halle.de

the magnonic dynamics may also trigger vortex motion resulting in combined dynamics of the order parameters in the SC/FM heterostructure. For a discussion of the use of SC/FM heterostructures for superconducting spintronic devices and for quantum computation, we refer the reader to the recent review article [27].

Here, we study fundamental aspects, specifically we are interested in the influence of superconducting correlation on the FM low-energy excitations (spin waves) in SC/FM layer structure. In particular, we focus on the dynamics of spin waves (magnons) in magnetic waveguides coupled to SC vortices. The potential of magnonic waveguides and spin waves in nanostructured magnets for low-energy magnon-based computing and data transfer have recently been demonstrated [33–42]. Introducing SC allows for new possibilities for data handling such as using supercurrents or SC vortices.

II. METHODS AND RESULTS

We consider a system consisting of a type II SC separated from a FM by an insulating spacer layer of thickness $h = 5$ nm, as shown schematically in Fig. 1(a), meaning a direct FM-SC hybridization or orbital reconstruction [18] are of less relevance. The determining factors are then the stray fields and possible drag or pinning effects that may change the damping properties of the FM excitations and SC vortex dynamics, especially in clean SC. For quantitative estimates, we performed numerical simulation for permalloy Py layer with the saturation magnetization

$M_s = 676$ kA/m, the exchange stiffness $A = 16$ pJ/m [26], and vanishing magnetocrystalline anisotropy. As the SC we use Nb with a magnetic penetration depth of $\lambda(8K) = 150$ nm [26], and a Ginzburg-Landau parameter $\kappa = 1$, which is a reasonable value for Nb in the clean limit [43]. The interaction of the spin waves or magnonic excitations in the FM planar waveguide with the superconducting vortices is simulated in two steps. At first, we solve for the dimensionless time-dependent Ginzburg-Landau (TDGL) equations [44]

$$\eta_1 \left(\frac{\partial \Psi}{\partial t} + i\kappa \phi \Psi \right) + \Psi (|\Psi|^2 - 1) + \left(\frac{1}{in\kappa} \nabla - n\mathbf{A} \right)^2 \Psi = 0, \quad (1)$$

$$\frac{1}{n} \nabla \times \nabla \times \mathbf{A} = -\eta_2 \left(n \frac{\partial \mathbf{A}}{\partial t} + \frac{1}{n} \nabla \phi \right) + \mathbf{j}_s, \quad (2)$$

$$\mathbf{j}_s = \frac{i}{2n\kappa} (\Psi \nabla \Psi^* - \Psi^* \nabla \Psi) - n|\Psi|^2 \mathbf{A}, \quad (3)$$

with the boundary condition

$$\left(\frac{1}{in\kappa} \nabla \Psi - n\Psi \mathbf{A} \right) \cdot \mathbf{N} = 0. \quad (4)$$

The solution of Eqs. (1)–(4) yields the distribution of the static equilibrium vortex lattice. In general, to capture all the facets of the coupled SC/FM dynamics (including the

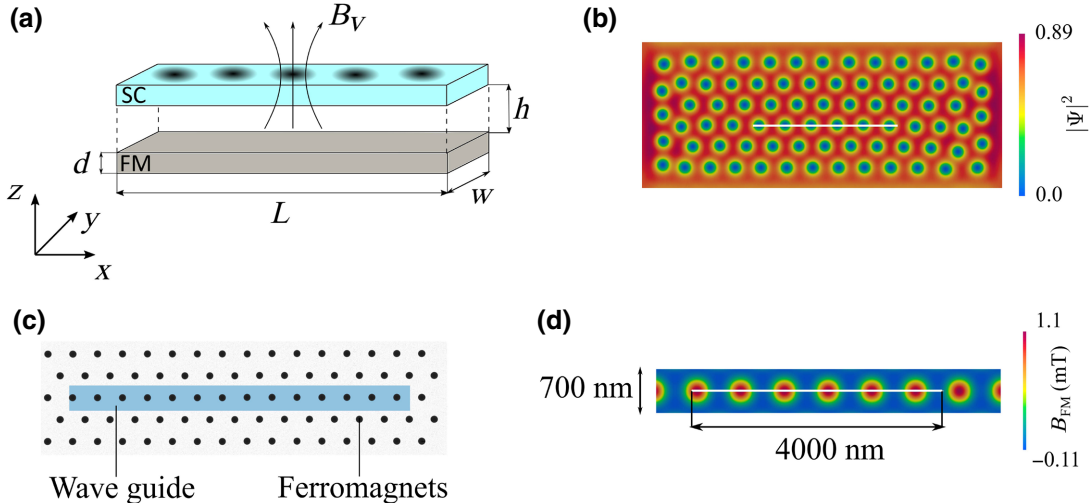


FIG. 1. (a) Schematics of the system under investigation. A type II SC reacts to an external magnetic field by forming vortices and modulating the spin wave dynamics in an attached ferromagnetic layer. (b) Simulation results of the TDGL equations for the spatial distribution of the amplitude $|\Psi|^2$ of the superconducting order parameter. A static external magnetic field was applied along the z direction with strength $B_z = 5$ mT. The blue regions are normal conducting and indicate the positions of vortex cores. (c) The field of the vortex lattice is modeled by the stray fields of ordered nanomagnets (black dots indicate the lateral positions of the nanomagnets). (d) Field distribution B_z in the magnonic planar waveguide, modulated by nanomagnets with magnetization $M_{s1} = 315$ kA/m. The lines in (b) and (d) indicate the regions over which line plots were taken.

back-action of both subsystems), a self-consistent solution of the TDGL and the Landau-Lifshitz-Gilbert (LLG) equations is required which is, in its full generality, a computationally formidable task (the LLG describes the magnetic dynamics). Indications of the effects of the stray fields of the magnonic systems on the SC ordering have been reported in [45]. Simulations and discussions on this issue in the context of the present work are presented in the Appendix. Furthermore, in principle, the static vortex lattice structure can be also calculated with the aid of the conventional time-independent Ginzburg-Landau (GL) equations. Here, we are interested in the stability, meaning the dynamics of the SC vortex structure, to external perturbations such as magnetic fields to excite the magnons as well as in the typical time scales of the SC dynamics compared with the magnonic time scale. In this paper, for brevity, we concentrate on the magnonic dynamics without discussing in depth the calculational results that convinced us the SC vortex lattice is stable while triggering and propagating the magnons. One example is shown in the Appendix for the response of the SC part of the system to the time-varying Oersted fields of the microwave antennas. Technically, the numerical solution of the classic GL equations is computationally more challenging than the solution of the TDGL system of Eqs. (1)–(4), although both systems of equations have the same equilibrium solution. Therefore, in this work the TDGL formalism is used throughout both to obtain the solution of the classic GL equations and for the SC dynamics.

From Eqs. (1)–(4) one obtains Ψ which is the superconducting order parameter. Here $|\Psi|^2 = n_s$ is the local density of Cooper pairs. The electric scalar potential ϕ is eliminated by choosing the gauge $\phi = 0$ [46]. The dynamic coefficients η_1 and η_2 as well as the spatial scaling parameter $n = L/\lambda$ with $L = 150$ nm result from the normalization of the equations (details of the scaling procedure can be found in the Appendix). Magnetic fields enter the formalism via their corresponding vector potentials $\mathbf{A} = \mathbf{A}_e + \mathbf{A}_{sc}$. Here $\mathbf{B}_e = \nabla \times \mathbf{A}_e$ is an external magnetic field which acts likewise on the SC and FM. Of primary interest for the following analysis are the supercurrents \mathbf{j}_s and the magnetic field $\mathbf{B}_{sc} = \nabla \times \mathbf{A}_{sc}$ which they produce.

In calculating the equilibrium state of the system, the magnetic self-field of the SC is neglected, that is, $\mathbf{A}_{sc} = 0$. This is a reasonable approximation if the SC is a thin layer of thickness $d \ll \lambda$ or in the high- κ limit, that is, $\kappa \gg 1$ [47,48]. Our aim is to run simulations mimicking the experiment [26] in which case the field in the SC is supposed to be dominated by the external field, meaning in this geometry the magnetostatic demagnetization fields are of less importance for the SC dynamics (in contrast to other geometries [28,29,49]). The vector potential that acts on Ψ is related to the external magnetic field by $\nabla \times \mathbf{A} = \nabla \times \mathbf{A}_e = \mathbf{B}_e$ with the gauge $\mathbf{A}_e = -B_e y \mathbf{e}_x$. We

use $\mathbf{B}_e = B_e \mathbf{e}_z$ with $B_e = 5$ mT. The technical details on how we solve for the first TDGL to find the equilibrium state of the SC (in the absence of the FM) have been presented elsewhere [28,29]. In principle, the bias field for the magnonic waveguide $\mathbf{B}_{\parallel} = 60$ mT \mathbf{e}_x also acts on the SC. We are considering, however, a thin film of thickness $d < \xi_{GL}$ and, therefore, the magnetic bias field (for the used strength) does not generate in-plane vortices [50], and it does not affect the equilibrium state of the SC, shown in Fig. 1(b). A further effect that appears, in general, is the influence of the dynamic demagnetization fields of the spin waves on the SC dynamics, an effect which we assume to be suppressed by the spacer layer (but we did not quantify this statement due to limited computational resources). Furthermore, the SC is assumed to be devoid of structural defects. The vortices tend therefore to form a hexagonal lattice [51], as evidenced by Fig. 1(b) where each of the blue dots corresponds to a vortex with normal conducting core surrounded by a whirl of supercurrents. The fields produced by these currents are used to modify the magnon dynamics in the adjacent FM, but their effect on the SC is assumed to be negligible.

To understand the effect of the static superconducting vortices on the magnons we compare with simulations where the vortex lattice is replaced by a static lattice of nanomagnets (cf. Fig. 1). We calculate then the stray fields [52] of the nanomagnets and compare with the magnetic fields B_v associated with SC vortices. The appropriate dimensions and geometry of the nanomagnets we infer from the equilibrium vortex lattice delivered as a solution of the TDGL equation. The magnetic fields are then used as input in micromagnetic simulations [53]. Simulations are performed and compared for the cuboid nanomagnetic replacement and the full solution of the coupled TDGL/micromagnetic systems. The field of a magnetic cuboid can be calculated analytically and its strength and spatial distribution are adapted to B_v [52]. The nanomagnets are chosen to have dimensions $\Delta x = \Delta y = 250$ nm and $\Delta z = 360$ nm and are placed under the magnonic waveguide with an air gap between the materials of $\Delta h = 175$ nm. Similarly to the vortices, the nanomagnet lattice has a hexagonal symmetry with a lattice constant of $c = 700$ nm [Fig. 1(c)]. To each nanomagnet we attach a magnetization $\mathbf{M} = M_{s1} \mathbf{e}_z$ with the saturation magnetization M_{s1} to be adjusted. For $M_{s1} = 315$ kA/m the field distribution in a magnonic stripe of width $w = 700$ nm is shown in Fig. 1(d). Similar to the vortices the nanomagnets produce a field with local maxima directly above each magnet. The fields are also compared via line plots along the x direction in the magnonic waveguide (Fig. 2). For a magnetization $M_{s1} = 12.6$ kA/m the fields are quite similar in magnitude and spatial extend. As the vortex lattice and the magnet lattice have slightly different lattice constants, the frequency of the field oscillations is not exactly the same. In our case, the lattice constant of

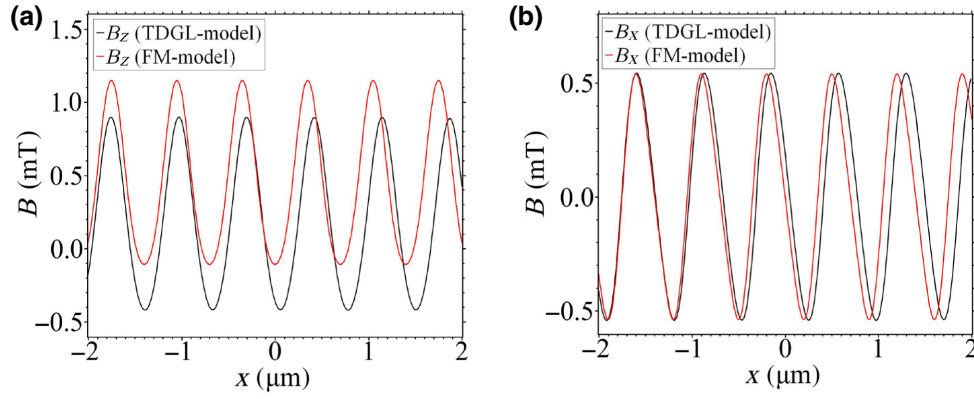


FIG. 2. Comparison of the vortex field as follows from the solution of the TDGL equations and the stray field of static cuboid nanomagnets (FM model) for $M_{s1} = 12.6$ kA/m along the lines indicated in Figs. 1(b) and 1(d).

the nanomagnets is chosen to be $c_m = 700$ nm, which is between the experimentally obtained value for the vortex lattice $a(B_{\perp} = 5$ mT) = 691 nm [26] and the simulated vortex lattice $c(B_{\perp} = 5$ mT) = 720 nm.

The magnon dynamics in the planar magnonic waveguide are inferred from the solution of the LLG equation

$$\frac{\partial \mathbf{M}}{\partial t} = \frac{\gamma^*}{1 + \alpha^2} (\mathbf{M} \times \mathbf{B}_{\text{eff}} + \alpha \mathbf{M} \times (\mathbf{M} \times \mathbf{B}_{\text{eff}})). \quad (5)$$

The effective field \mathbf{B}_{eff} follows from the functional derivative of the magnetic free energy density with respect to the magnetization and γ^* is the gyromagnetic ratio. The LLG equation is solved via the micromagnetic simulation program MuMax3 [53].

The magnonic waveguide is a Py stripe of width w , thickness $d = 1$ nm, and length $L = 28$ μm . The material parameters are as indicated previously and we use a unit cell size of $5 \times 5 \times 1$ nm³. Spin waves are excited by applying a sinc-field $\mathbf{H} = H_0 \sin(2\pi ft)/(2\pi ft) \mathbf{e}_y$ with $H_0 = 15$ mT and $f = 20$ GHz to a 5-nm-long stripe at the center of the waveguide and across its width. As in the experiment [26], bias fields $H_{\parallel} = 60$ mT and $H_{\perp} = 5$ mT are applied to the waveguide to set the magnon propagation into a backward volume magnetostatic spin-wave (BVMSW) configuration. The perpendicular field here is necessary to generate vortices in the adjacent SC but otherwise, in all shown simulations, it did not have any observable effect on the results. Spin-wave spectra are obtained by applying a 2D fast-Fourier transform (FFT) to the magnetization fluctuation $\delta m_z(x, t)$ along the center of the waveguide [54]. As the artificial vortex field acting upon the magnetization is rather weak, the band gaps are expected to be on the order of MHz and below. Therefore, long simulation times are required in order to obtain dispersion plots with sufficiently good resolution. We neglected in the calculations the magnetic damping, after assuring that its influence on the magnon dynamics for $\alpha \leq 10^{-3}$ does not change the dispersion, except

for the usual damping-induced blurring of the dispersion branches (if α is assumed local and static, i.e., independent of frequency and wave vector).

III. MAGNON DISPERSION CAUSED BY SUPERCONDUCTING VORTICES

The nanomagnets saturation magnetization is $M_{s0} = 12.6$ kA/m. Their stray fields form a lattice that matches well the field of the SC vortex lattice (see Fig. 2). We ramp up the magnetization to $M_{s0} = 25M_{s1} = 315$ kA/m which allows for a better insight into the characteristics of the magnonic dispersion. The magnon dispersion curves for $M_{s1} = 0$ and $M_{s1} = 25M_{s0}$ are shown in Fig. 3(a). In the absence of SC vortices, the dispersion exhibits a typical BVMSW behavior with a dominant first-order mode and a weaker higher-order mode [55–58]. As the waveguide is relatively thin, the dispersion is dominated by exchange-type magnons and the k -space region with negative group velocity is very narrow. No band gaps are observed except for the intrinsic gap $f < 6.62$ GHz due to the external bias field and the finite width of the waveguide. The shift of the bands to higher frequencies is known to be of purely dipolar origin and can be explained by an effective pinning of the dynamic magnetization component at the lateral edges of the stripe [59,60]. When switching on the vortex field (amounts to $M_{s1} = 25M_{s0}$), band gaps appear at wave vectors $k = n\pi/c_m$, $n \in \mathbb{Z}$ [Fig. 3(b)]. The opening of gaps at the edges of the Brillouin zones (BZs; thick green lines) upon the formation of standing wave patterns in periodic systems (due to interference of incoming and partially reflected waves) is well established in magnonics [55,56], photonics [61], and electronic systems. Higher bands display gaps that open not at the BZ boundary but also inside the BZs (vertical dashed lines). The existence of these bands can be understood by considering that it is not only the first-order modes that propagate inside the waveguide but also higher-order width modes are excited, as displayed in Fig. 3(a). The higher-order modes are also reflected by

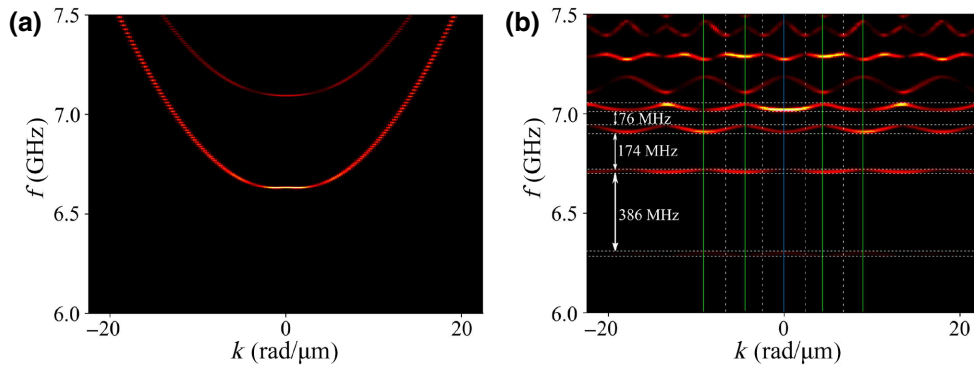


FIG. 3. Influence of the vortex lattice on the magnon dispersion. (a) Dispersion relation in the absence of vortices ($M_{s1} = 0$). (b) Modified dispersion relation for an artificial vortex lattice composed of nanomagnets with magnetization $M_{s1} = 25M_{s0} = 315$ kA/m.

the vortex field and their interaction with the lowest-order mode leads to more complicated standing wave patterns and the formation of additional band gaps. This behavior is known from width-modulated magnonic crystals where the higher-order modes are excited by magnonic scattering at edge steps in the waveguide [62,63]. Another feature of our dispersion relation is the existence of a band at $f = 6.3$ GHz inside the formerly forbidden region $f < 6.62$ GHz.

For an insight into the mechanism that allows spin waves to propagate in this region, we calculated a band gap diagram of the waveguide for different strengths of the vortex field. In addition, we also allowed for different sizes of the air gap between the nanomagnets and the waveguide. The results are shown in Fig. 4(a), which provides evidence that with increasing strength of the vortex field several band gaps open (white), whereas for zero field all frequencies with $f > 6.62$ GHz can propagate (gray). The lowest allowed band for all field strengths is almost flat and its central frequency is shifted downwards with increasing M_{s1} . The second allowed band displays a similar behavior but the frequency shift is less obvious. The modified

dispersion characteristics become more pronounced if the distance between the nanomagnets and the waveguide is reduced to $h = 100$ nm [cf. Fig. 4(b)]. In this case the amplitude of the field modulation in the waveguide is stronger, which has a similar effect as increasing M_{s1} to a higher value. The reduced air gap size drives the opening of the band gaps even further. In addition, the bands show a stronger downwards shift, even for higher frequencies. The number of flat bands also increases. Apart from these differences, the dispersion diagrams show a very similar behavior which indicates that the two experimentally observed band gaps stem from the magnon modes at the top and bottom surfaces of the waveguide. Comparing the frequency spectra in Figs. 3(b) and 4, we infer that the frequency band at $f = 6.3$ GHz is the lowest-order band shifted downwards by the vortex field. It should be noted that for $h = 175$ nm the first three allowed bands are not affected by the higher-order modes, whereas for $f > 7$ GHz anticrossing between branches of the first mode and the higher modes leads to a more complicated band structure. In the case of $M_{s1} = 1M_{s0}$, which is a realistic vortex field strength, only a single band gap of width $\Delta f \approx$

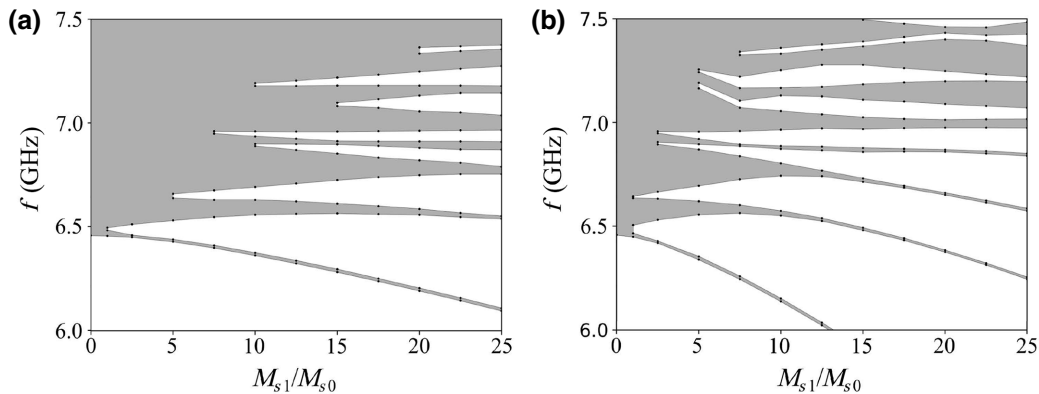


FIG. 4. Frequency diagrams for a strip of width $w = 700$ nm and different ratios M_{s1}/M_{s0} . White corresponds to band gaps and gray corresponds to allowed frequencies. The air gap between the waveguide and the nanomagnets is chosen to be (a) $h = 175$ nm and (b) $h = 100$ nm.

18 MHz appears in the dispersion relation. This magnonic gap is much smaller than that reported in the experiment of Dobrovolskiy *et al.* [26], where $\Delta f \approx 50$ MHz. Possible reasons for this discrepancy are addressed in the following.

IV. EFFECT OF THE THICKNESS OF THE WAVEGUIDE

Studying how the thickness h_{FM} of the waveguide affects the magnonic dispersion, the width of the FM is set to $w = 65$ nm and the length $L = 28$ μm remains as before. In addition the magnetization of the nanomagnets is kept at $M_{s1} = 1M_{s0}$. The reduced value of w increases the mode quantization and shifts the higher-order modes to higher frequencies. In our case the frequency shift is large enough for the second mode to disappear completely from the dispersion plots. The second important geometry effect is related to the variable thickness of the waveguide. In previous calculations the FM thickness had the relatively small value of $d = 1$ nm, which leads to a strongly exchange-dominated dispersion relation. As d is increased, the ferromagnetic volume increases and the dipolar interactions become of a greater importance. It is therefore to be expected that the typical BVMSW behavior of the magnons becomes more visible for larger d . In Figs. 5(a) and 5(b) the width and the center frequencies of the appearing band gaps are displayed in dependence of

h_{FM} . Apparently only two band gaps appear when varying the FM thickness and the gap width is in the MHz range. For $h_{\text{FM}} = 1$ nm the only band gap has now a width of $\Delta f \approx 23$ MHz, which is slightly larger than the gap width of the waveguide with $w = 700$ nm. As the FM thickness is increased the gap width decreases until the band disappears completely at $h_{\text{FM}} = 7.5$ nm. Here, it should be noted that band gaps $\Delta f = 2$ MHz and below can no longer be determined accurately because the resolution in frequency space is limited by the simulation time (see, e.g., [54]). The increasing width of the waveguide not only leads to the opening of a second band gap, but the dipolar interactions also become of greater importance for the magnon dynamics. As a consequence the entire band structure is lifted upwards in frequency space [cf. Fig. 5(b)]. In addition, the region in k space for which the group velocity of the modes is negative increases. For $h_{\text{FM}} = 5.5$ nm this region stretches over the entire first BZ. For larger waveguide thickness, the first band gap disappears completely and only the second band remains finite [cf. Fig. 5(d)]. In this regime the BVMSW behavior of the magnons is clearly visible. Notably, a partial band gap opens at the first BZ boundary but does not prevail over the entire k space (gray bar). In addition, a second band gap opens at unconventional k values (dashed vertical lines). The nature of these features becomes clearer by applying a logarithmic color scale to the dispersion relation, as can be seen

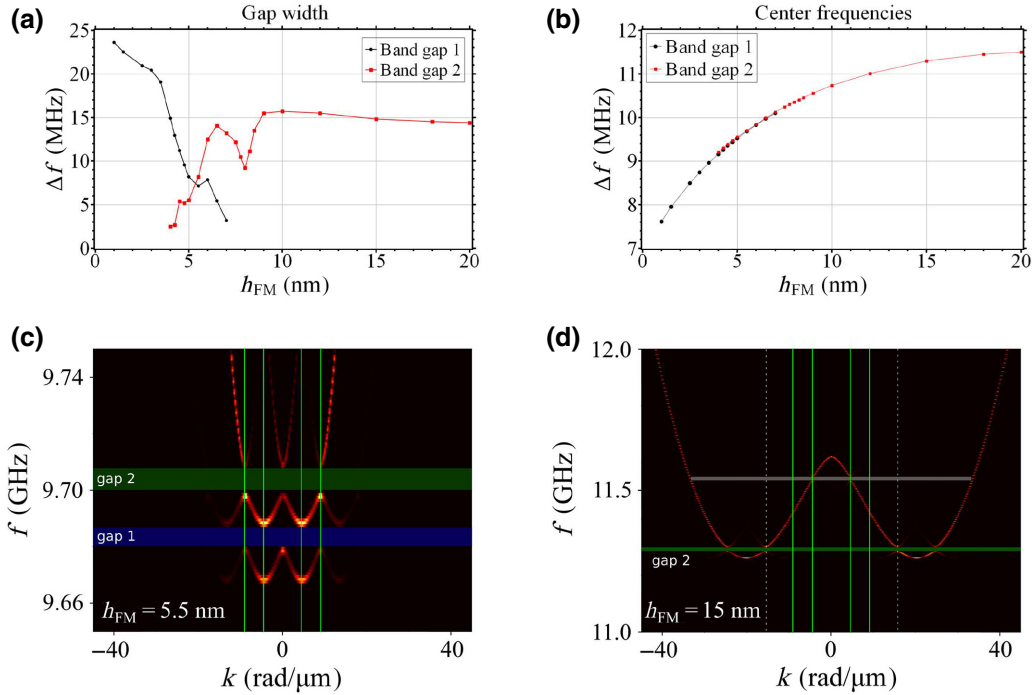


FIG. 5. Influence of the waveguide thickness h_{FM} on the magnon dispersion for $M_{s0} = 1M_{s0}$. The waveguide has a width of $w = 65$ nm and an air gap size of $h = 175$ nm. (a), (b) Width and center frequencies of the band gaps appearing in the dispersion relation, respectively. (c), (d) Magnonic dispersion for $h_{\text{FM}} = 5.5$ nm and $h_{\text{FM}} = 15$ nm, respectively. Thick green lines indicate the edges of the first two BZs. Dashed lines indicate unconventional k values at which gaps open.

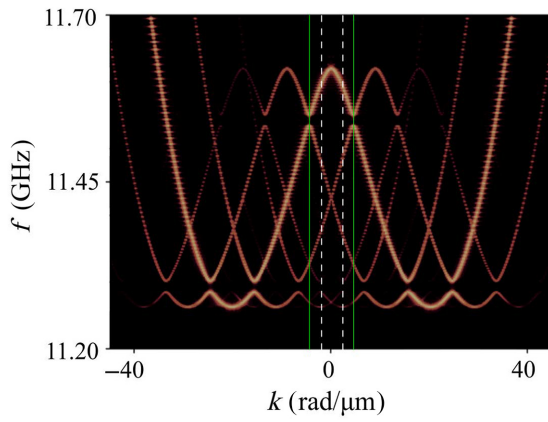


FIG. 6. Magnonic dispersion for $h_{\text{FM}} = 15$ nm and logarithmic color scale [cf. Fig. 5(d)]. Thick green lines indicate the edge of the first BZ and dashed lines indicate k values $k = \pm 0.5\pi/c$ at which gaps open.

in Fig. 6. Apparently the second band gap already opens at k values $k = \pm 0.5\pi/c$ and stretches over the entire k space. In contrast, the gap opening at the first BZ boundary $k = \pm\pi/c$ is incomplete and only modes with negative group velocity are affected by the presence of the vortices. It should also be noted that modes with $k = \pm 2\pi/c$ can travel undisturbed through the waveguide and there is no gap formation in this frequency regime. The reason for this behavior is still under investigation and will not be addressed further in this work. These results show that the waveguide geometry is an important factor in the problem and should be taken into account when comparing theory and experiment.

V. DISORDERED VORTEX LATTICE

How does an imperfect vortex lattice affect the magnon propagation? To address this issue, two kinds of disorder are used. First the vortices are allowed to have random field values at each location. This particular kind of disorder corresponds to the case of a SC with varying GL parameter κ . In a perfectly homogeneous superconducting film the electronic mean free path l as well as the film thickness are uniform leading to a constant value of κ . However, variations in either of these parameters make κ a space-dependent quantity. For instance, it was predicted that in a superconducting wedge the effective GL parameter is modified via a thickness gradient along the sample [64]. This geometric modification of κ allows for the formation of vortices and enabled a study of the dependency of the vortex field strength on the value of κ . It is shown that the vortex field becomes considerably weaker as the thickness of the sample is reduced and the GL parameter is increased. In samples with thickness variations, vortices are thus expected to have a field strength that depends on the position in the sample. On the other hand, it is also known that

vortices prefer to reside at positions with reduced thickness because the volume filled with supercurrent is reduced in this way lowering the energy. Random thickness variations are also expected to lead to some degree of structural disorder in the vortex lattice. Variations in the electronic mean free path have a similar effect and can modify the London penetration depth λ as well as the GL parameter [1,65]. In real SCs the nonuniformity of the sample geometry and compositions usually hinder the formation of a perfectly hexagonal vortex lattice. Therefore, it is instructive to investigate how magnon-fluxon interaction is affected by this phenomenon. For clarity, the field variations and the spatial disorder are investigated independently.

A. Variations of the field strength

The effect of varying the field strength on the magnon dispersion is investigated with the system displayed in Fig. 7(a). The FM geometry is that displayed in Fig. 1, that is, we have $w = 700$ nm, $h_{\text{FM}} = 1$ nm, $L = 28$ μm , and an air gap size of $h = 175$ nm. The vortices can form a perfectly hexagonal lattice but their corresponding field strength varies from position to position. This field variation is introduced in our artificial model by allowing the magnetization of the nanomagnets to vary randomly in a certain interval $M_{s1} - \Delta M, M_{s1} + \Delta M$. Here M_{s1} is the saturation magnetization in the absence of disorder.

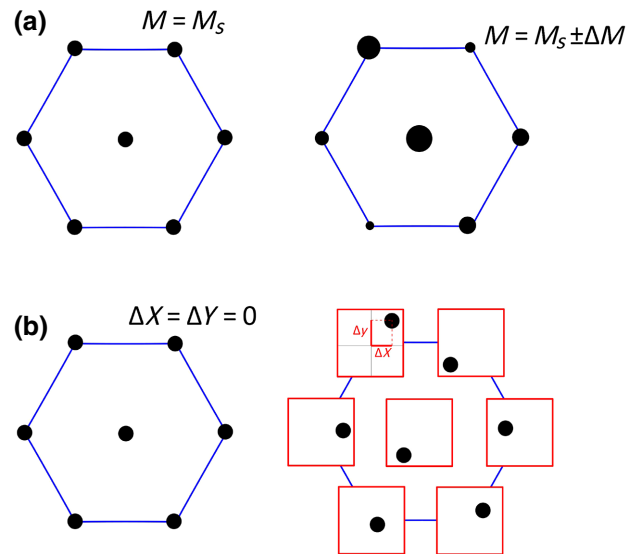


FIG. 7. Schematic of the two kinds of disorder of the vortex lattice. (a) The vortex lattice with perfect structural order but varying field strength between the vortices. The field variation is introduced by random magnetizations of the nanomagnets in the interval $[0.85M_{s1}, 1.15M_{s1}]$ or $[0.7M_{s1}, 1.3M_{s1}]$ with saturation magnetization $M_{s1} = 3.5M_{s0} = 44.1$ kA/m. (b) All nanomagnets are magnetized equally strong. They occupy random locations in a box of side length $a = 100$ nm or $a = 200$ nm around their ideal position.

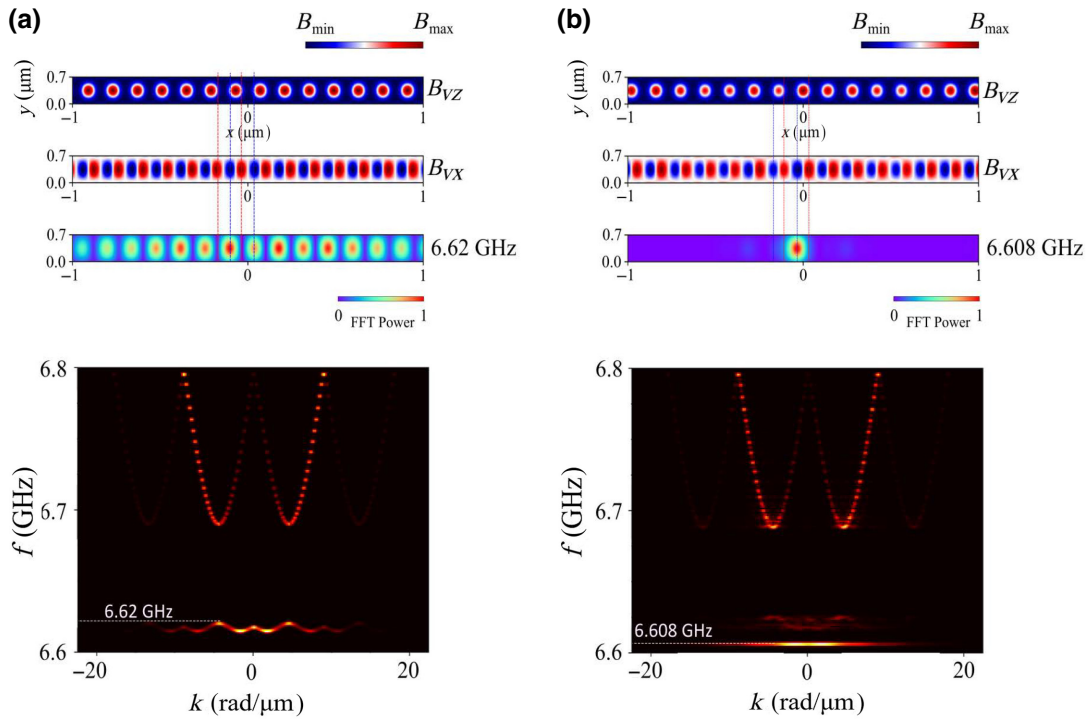


FIG. 8. Magnonic dispersion and mode profiles (a) in the absence of disorder and (b) for a disordered vortex lattice. Disorder is introduced via a varying field strength where the magnetization has random values in the interval $[0.85M_{s1}, 1.15M_{s1}]$. Here B_{vx} and B_{vz} correspond to the field components of the vortex field B_v . Blue and red dashed vertical lines correspond to the positions of the minimal and maximal total static magnetic field, respectively.

In previous calculations we had $M_{s1} = 12.6$ kA/m which resulted in the formation of band gaps on the order of $\Delta f \approx 18$ MHz. Choosing $M_{s1} = 44.2$ kA/m leads to the formation of band gaps of $\Delta f \approx 60$ MHz. This value fits the experiment by Dobrovolskiy *et al.* [26] better than predicted by our GL simulations. Three calculations were performed, one with uniform magnetization and two others in which the magnetization was allowed to have random values in the interval $[M_{s1} - 0.15M_{s1}, M_{s1} + 0.15M_{s1}]$ or $[M_{s1} - 0.3M_{s1}, M_{s1} + 0.3M_{s1}]$. The results for 15% variations in the field strength are displayed in Fig. 8. A more detailed overview on the mode profiles, including the case of strong disorder, is shown in Figs. 9–11. In the absence of disorder, the dispersion develops a number of allowed and forbidden gaps which open at the BZ boundaries, as discussed in the preceding sections. Here, two band gaps appear having the widths of $\Delta f = 65$ MHz and $\Delta f = 12$ MHz (not shown here). The lowest-order band has a small but finite dispersion. As disorder is introduced into the system this dispersion quickly disappears and the band flattens out. It can also be observed that an additional number of flat bands appear above the initial band. The band gap is therefore reduced to some extent.

To understand the origin of the additional flat bands, we calculated the Fourier amplitudes of the magnonic modes

for a number of selected frequencies and different levels of disorder (see Figs. 8–11).

Under the uniformly magnetized lattice, the lowest-order modes are predominantly located at positions where the vortex field counteracts the external bias field. At these positions, the total magnetic field has local minima and the energy of the modes at these positions is reduced. This mode confinement affects also the magnonic dispersion and partially inhibits mode propagation, because the propagation and the dispersion are inherently coupled. In contrast, higher-frequency modes are also located at the positions where the total magnetic field has local maxima. The flattening of the lowest-order band has been discussed previously. Now it is evident that increasing the magnetization of the nanomagnets goes hand in hand with a confinement of the magnonic modes above the positions of the magnets. By increasing the field strength, the mode propagation becomes increasingly inhibited and the lowest band turns flat and is shifted towards lower frequencies. A very similar behavior is known to occur in surface-modulated magnonic crystals [66]. Here, a periodic magnetic field modulation is introduced into the system by carving grooves into the surface of the waveguide. The static stray field of these surface defects leads to similar field variations and mode confinement, as in our system. Flat bands have also been observed in magnonic crystals

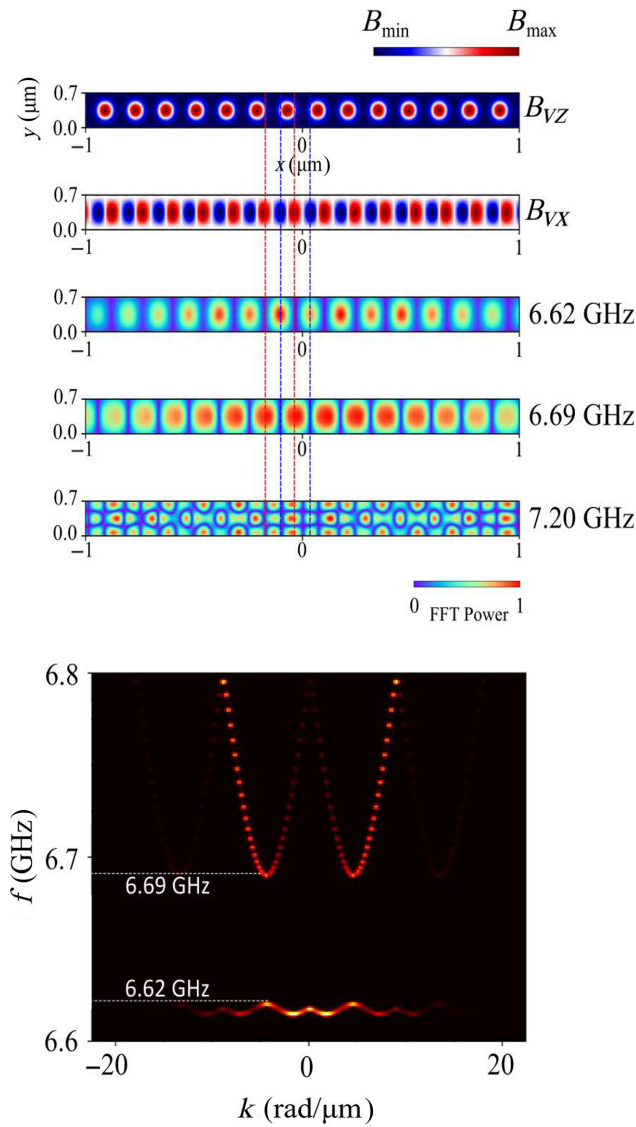


FIG. 9. Mode profiles for selected frequencies in the absence of disorder. Here B_{vx} and B_{vz} correspond to the field components of the vortex field B_v . Blue and red dashed vertical lines correspond to the positions of the minimal and maximal total static magnetic field, respectively.

with periodic Dzyaloshinskii-Moriya interaction [67]. For a given magnetization of the nanomagnets, the mode propagation in our system is inhibited but not zero. When the field is allowed to vary between different nanomagnets, even for field variations of 15%, the lowest-order band becomes completely flat. By inspecting the mode profiles of the corresponding frequencies, we deduce that the flat modes correspond essentially to knots above certain vortex positions. The oscillations of these knots is no longer coherent and uniformly propagating waves cannot form. With increasing variation of the field strength of the nanomagnets, this effect becomes more prominent and more flat bands appear. Higher-frequency modes are much less

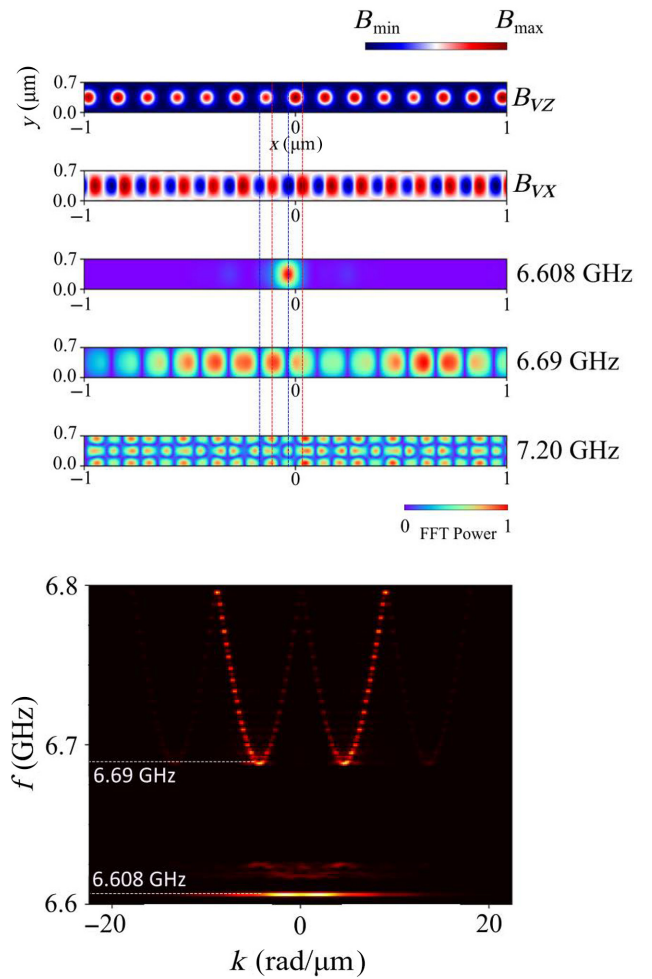


FIG. 10. Mode profiles for selected frequencies. Disorder is introduced via a varying field strength. The magnetization has random values in the interval $[0.85M_{s1}, 1.15M_{s1}]$. Here B_{vx} and B_{vz} correspond to the field components of the vortex field B_v . Blue and red dashed vertical lines correspond to the positions of the minimal and maximal total static magnetic field, respectively.

affected by the variations in the field strength because they are mostly exchange driven.

B. Variations in field position

To study the vortex lattice with structural disorder, the nanomagnets are assumed to all have the same magnetization. Allowing the nanomagnets to occupy random positions had a similar effect as the variations in their field strength. Essentially the lowest-order mode can no longer form coherently and magnon propagation is not possible. This again leads to the formation of a number of flat bands in the dispersion relation, as demonstrated by Figs. 12 and 13. However, in this case the higher-frequency bands are much more strongly affected by the disorder in the system. This becomes particularly clear for high structural disorder where vortices are allowed to occupy

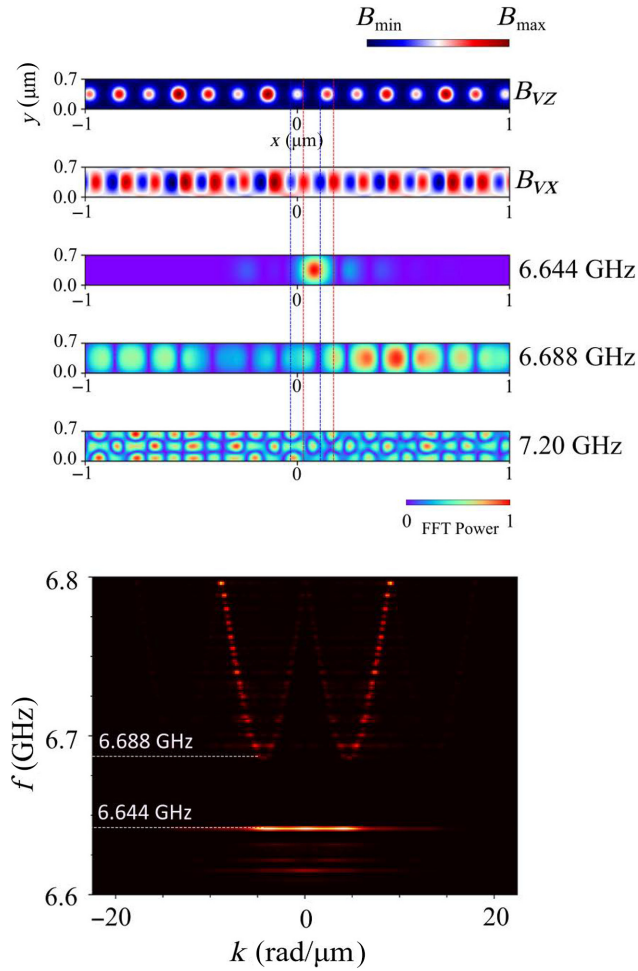


FIG. 11. Mode profiles for selected frequencies. Disorder is introduced via a varying field strength. The magnetization has random values in the interval $[0.7M_{s1}, 1.3M_{s1}]$. Here B_{vx} and B_{vz} correspond to the field components of the vortex field B_v . Blue and red dashed vertical lines correspond to the positions of the minimal and maximal total static magnetic field, respectively.

random positions in a box with side length $a = 200$ nm. Here, the lower part of the second allowed band is completely cut off and the band edge is replaced by another flat dispersion branch. In addition, the mode profile of the frequency $f = 7.2$ GHz is strongly modified compared with the previous cases.

VI. SUMMARY AND COMPARISON WITH EXPERIMENT

We presented a framework for capturing the magnonic-superconducting dynamics in a proximity-coupled ferromagnetic/type II SC hybrid structure. The magnonic dispersion depends markedly on the details of the superconducting excitations. A number of aspects remain to be investigated and included in the theory which can be best inferred by contrasting with experiment: comparing our

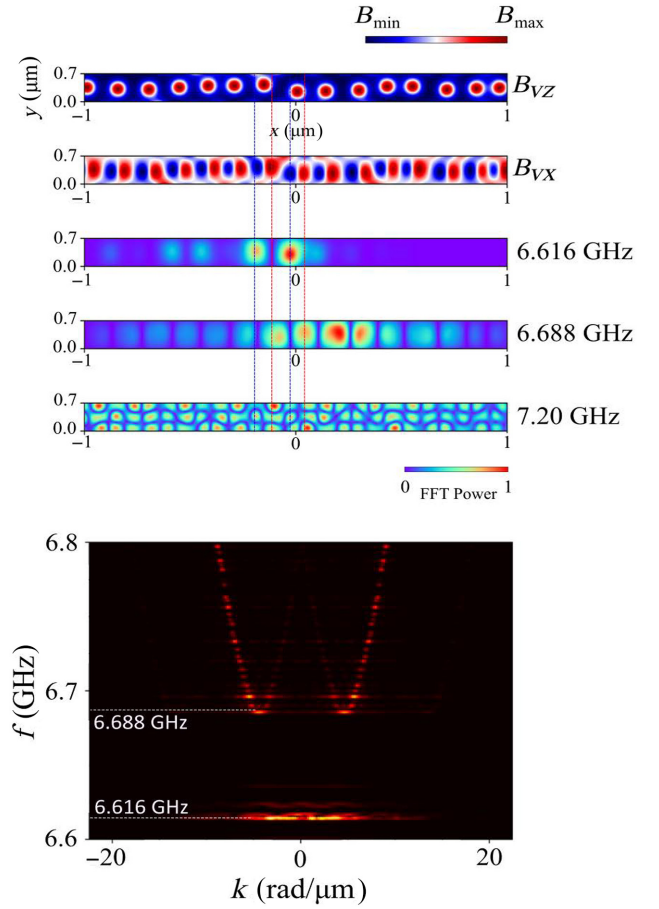


FIG. 12. Mode profiles for selected frequencies. Disorder is introduced by varying the vortex positions. The vortices are randomly located in a box of side length $a = 100$ nm. Here B_{vx} and B_{vz} correspond to the field components of the vortex field B_v .

results to the experiments reported by Dobrovolskiy *et al.* [26] we find that the experiment is matched best when we use the same material parameters as in the experiment and the vortex field is $B_{\perp} = 5$ mT with the whole system having a comparable size to the experiment. Our simulations confirm the existence of band gaps in the magnonic spectra due to the presence of a hexagonal vortex lattice in the SC. The vortex field is observed to act as a Bragg grating that leads to the opening of band gaps at the BZ boundaries $k = n\pi/a_{VL}$, $n = 0, 1, \dots$ in the magnonic dispersion relation. In our calculations the in-plane component $B_{\parallel} = B_{vx}$ of the field is observed to have the greatest effect on the magnon dynamics whereas $B_{\perp} = B_{vz}$ did not visibly change the dispersion, even for artificially strong vortex fields. Quantitatively, our results do not match the experiment accurately. For a strength of the vortex field $M_{s1} = M_{s0}$, only a single additional band gap in the dispersion relation of the waveguide with $w = 700$ nm is observed. The band width is $f_{BG} = 18$ MHz, which is much smaller than the band width in the experiment where $f_{BG} = 50$ MHz. If the strip width is increased to $w = 2 \mu\text{m}$,

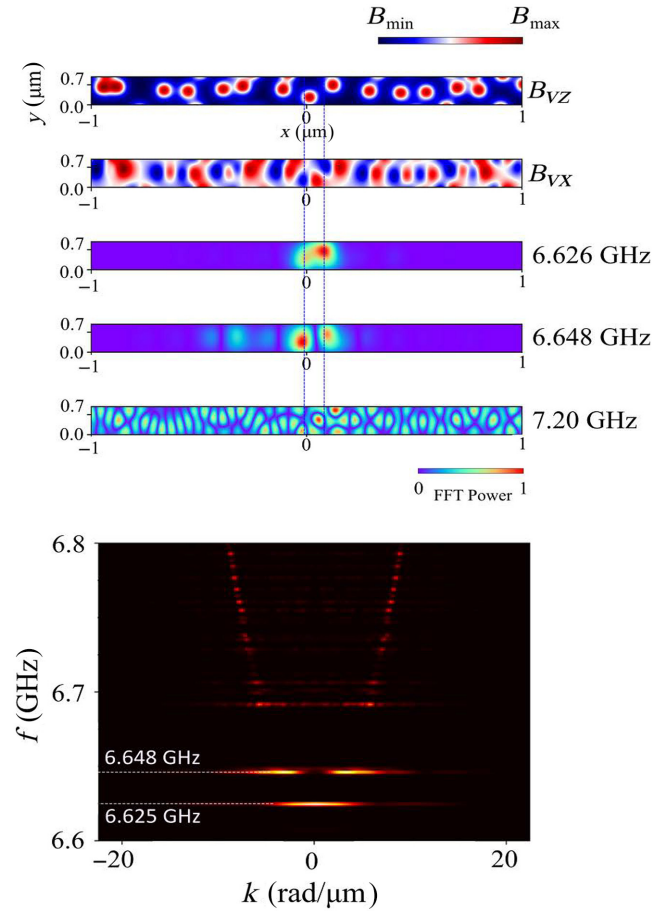


FIG. 13. Mode profiles for selected frequencies. Disorder is introduced by varying the vortex positions. The vortices are randomly located in a box of side length $a = 200$ nm. Here B_{vx} and B_{vz} correspond to the field components of the vortex field B_v .

the same as in the experiment, the band gap becomes so small that it can no longer be detected with our methods. This means in the experiment that the vortex field is either stronger than in our case or the downward shift of the lowest band is more extreme. In our calculations we neglected the influence of the superconducting stray fields on the SC itself, and a following modification of the supercurrent distribution in the SC. The vortex field would also be affected by this modification. It could also be that our GL parameters are not a perfect match to the system used in the experiment. It should also be noted that we used a waveguide of thickness $d = 1$ nm whereas in the experiment the thickness is $d = 80$ nm. Nonetheless, our results show that the geometry of the waveguide does not only affect the number of band gaps but also their width and position in Fourier space. In addition, because the vortex field is highly nonhomogeneous in space, the magnon propagation at the top and bottom layers of the waveguide are expected to be affected differently by the vortex field. Finally, we did not take into account the dynamic

interaction between the magnons and the vortices via their corresponding stray fields. This includes also the modification of the magnonic spectrum by the conventional Meißner screening of the SC; that is, it is known that the modification of the magnonic stray fields by the SC goes hand in hand with enhanced phase velocities and nonreciprocal behavior [68,69].

ACKNOWLEDGMENTS

We thank O. Dobrovolskiy and M. Krawczyk for stimulating discussions and the DFG for financial support through project No. 465098690.

APPENDIX: RESPONSE OF THE VORTEX LATTICE TO TIME-VARYING EXTERNAL FIELDS

The time-varying external field of the microwave antenna which is applied to generate magnonic excitations in the FM layer may affect the superconducting dynamics. A strong perturbation of the SC may invalidate the scenario that magnonic excitations evolve in the static magnetic field lattice due to the presence of the SC vortices (same applies to the effects of the dynamic demagnetization fields of the spin waves). For a quantitative insight into such effects (and also to study the SC/magnonic time-scale separations), we consider the dynamics of the vortex lattice in Fig. 1 in the time-varying Oersted field of the microwave antenna. Two settings for the system constituents are considered. The first setup is shown in Fig. 14. It corresponds to the system that is used for the calculations in the main text. In this setup, both FM and SC are separated by an insulating spaces layer and the antenna is placed above this hybrid structure. The second setup (cf. Fig. 15) corresponds to the experimental situation described by Dobrovolskiy *et al.* [26]. Here, the microwave antenna and the SC have a lateral distance of $d = 500$ nm and both are placed $h = 5$ nm above the FM. The discussion of dynamic processes in the SC requires a self-consistent solution of the TDGL equations (1)–(4). Here the following scaling is applied: $\Psi = \tilde{\Psi}\sqrt{|\alpha|/\beta}$, $\mathbf{A} = \tilde{\mathbf{A}}\hbar L/(q_s\lambda\xi)$, $\phi = \tilde{\phi}\kappa\hbar/(q_s\tau)$, $\nabla = \tilde{\nabla}/L$, and $\mathbf{j}_s = \tilde{\mathbf{j}}_s\hbar/(q_s\xi(T_0)\lambda(T_0)^2\mu_0)$. The quantities without tilde are the original expressions whereas the quantities with tilde are dimensionless. For clarity, the tilde was dropped later on. The scaling parameters are set to $\tau = 1$ ps and $L = 150$ nm. The mass and charge of a Cooper pair are denoted as m_s and q_s , respectively. For the dynamic coefficients following relations apply

$$\eta_1 = \frac{\xi(T_0)^2}{D\tau} = 3.916, \quad (\text{A1})$$

$$\eta_2 = \frac{\sigma\mu_0\lambda(T_0)^2}{\tau} = 2.184. \quad (\text{A2})$$

Hereby we adopted the commonly used model for the electric conductivity [70]

$$\sigma = \frac{l}{3.72 * 10^{-16} \Omega m^2} = 7.723 * 10^7 / (\Omega m). \quad (\text{A3})$$

The electronic mean free path is chosen as $l = 28.73$ nm, which is in accordance with the two-fluid model [1]

$$\lambda(T_0) = \lambda_L(T=0) \sqrt{1 - \left(\frac{T_0}{T_c}\right)^4}^{-1} \sqrt{1 + \frac{\xi_0}{l}} = 150 \text{ nm}. \quad (\text{A4})$$

We use the material parameters for Nb and operate at the temperature $T_0 = 0.9T_c$. Specifically, the critical temperature is $T_c = 9$ K, the London penetration depth at zero temperature is $\lambda_L(0) = 43$ nm, the Bardeen-Cooper-Schrieffer (BCS) coherence length is $\xi_0 = 91.5$ nm, and the Fermi velocity is $v_f = 6 \times 10^5$ m/s [71]. The diffusion coefficient in (A1) has the value $D = v_f l / 3 = 1.72 \times 10^{-2}$. As in the main text, we neglect the influence of the stray fields of the SC. However, because the external field is no longer changing adiabatically it is no longer permitted to simultaneously set $\mathbf{A}_{sc} = 0$ and $\phi = 0$. Instead, the electric scalar potential is solved by applying the divergence to Eq. (2) which results in

$$\eta_2 \Delta \phi = \nabla \cdot \mathbf{j}_s. \quad (\text{A5})$$

For the excitation field of the microwave antenna, we use the vector potential of an infinitely long cylinder carrying a uniform current I . This field can be calculated as

$$\mathbf{A}_a = B_0 d \log \left(\frac{\sqrt{(x-x_0)^2 + (z-z_0)^2}}{R} \right) \mathbf{e}_y. \quad (\text{A6})$$

In our case the cylinder has a radius of $R = 100$ nm and its main axis is parallel to the y axis. The constants x_0 and z_0 are chosen to match the configurations displayed in Figs. 14 and 15. The constant d is chosen such that the x component of $\mathbf{B}_a = \nabla \times \mathbf{A}_a$ has the defined value B_{0x} at the center of the FM film directly underneath the antenna position. A time-dependent signal can be constructed by multiplying (A6) with a time-dependent function $a(t)$. In our case, we use a sinc-pulse $a(t) = \sin(2\pi f(t-t_0)) / (2\pi f(t-t_0))$ with $f = 20$ GHz and $t_0 = 100$ ps. Before discussing the results, it is worth mentioning that the excitation field in the main text did not have a physically accurate form and is only chosen for convenient implementation. Simulations performed with the accurate field (A6) are confirmed to yield results which are identical to those already presented.

In Fig. 14 it is shown how the SC reacts to the time-varying Oersted field of the microwave antenna (setup

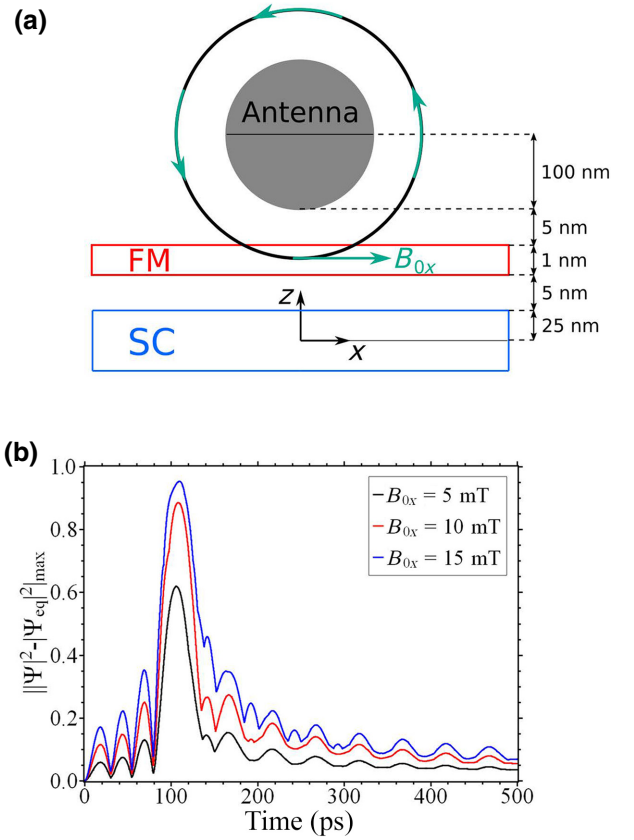


FIG. 14. (a) Setup used for the calculations in the main text. The Oersted field \mathbf{B}_0 of the antenna is set to have a maximum value B_{0x} at the center of the ferromagnetic film at $t = 100$ ps. The coordinate origin is located at the center of the SC. The excitation signal for magnons has the form of a sinc-pulse. (b) Maximum distortion $|\Psi|^2 - |\Psi_{eq}|^2|_{\max}$ of the vortex lattice where $|\Psi_{eq}|^2$ is the equilibrium order parameter distribution which is shown in Fig. 1.

1). For these simulations we use the parameter $\chi(t) = |\Psi(\mathbf{r}, t)|^2 - |\Psi_{eq}(\mathbf{r})|^2|_{\max}$ as a measure for the dislocation of the vortices. The subscript max indicates the spatial maximum value of the quantity in brackets. Before the excitation signal is switched on, the SC is in the equilibrium state which is displayed in Fig. 1. The corresponding order parameter is denoted as Ψ_{eq} . In Fig. 14(b) one observes that excitation fields of varying amplitudes lead to qualitatively similar results. Specifically, at $t_0 = 100$ ps, when $a(t_0) = 1$ the vortex lattice experiences the greatest disturbance and relaxes back slowly to the equilibrium once the field diminished. According to the way in which $\chi(t)$ is defined, a value $\chi = 1$ corresponds to a deflection of the vortices which is equal or larger than half of the lattice parameter $c = 700$ nm. A value $\chi > 1$ is not possible because $|\Psi|^2 \leq 1$. For the configuration displayed in Fig. 14(b) the vortex number is conserved for field amplitudes up to $B_{0x} = 15$ mT. Results for fields of significantly

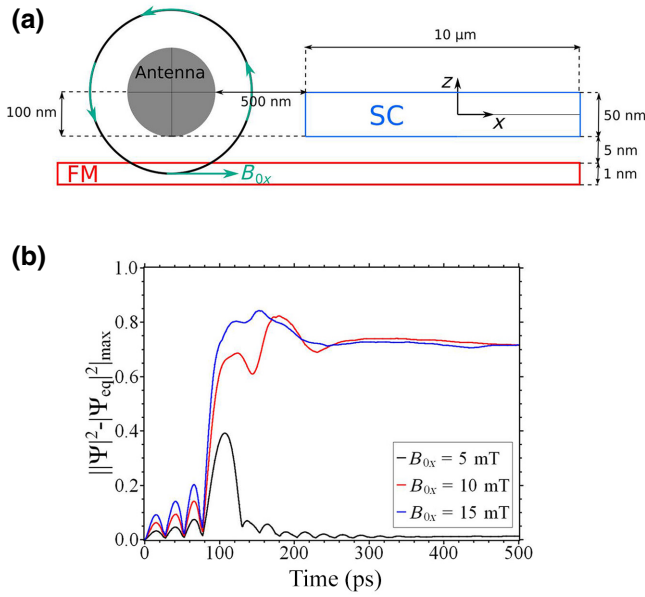


FIG. 15. (a) Experimental setup for studying the interaction between magnons and superconducting vortices. At $t = 100$ ps, the Oersted field \mathbf{B}_0 of the antenna has a maximum value B_{0x} at the ferromagnetic film center (which is also the origin of the coordinate system). Magnons are excited with a sinc-pulse. (b) Maximum distortion $|\Psi|^2 - |\Psi_{\text{eq}}|^2|_{\text{max}}$ of the vortex lattice where $|\Psi_{\text{eq}}|^2$ is the equilibrium order parameter distribution that is shown in Fig. 1.

larger amplitude (not shown here) can lead to different results in which case the physics of the SC/magnonic dynamics changes qualitatively.

The situation is different if we consider the setup shown in Fig. 15. Despite the larger distance between the antenna and the SC surface, already fields of amplitude $B_{0x} = 9$ mT are found to change the vortex number in the SC permanently. This change is also indicated by a permanent nonzero value of χ for times larger than $t_0 = 100$ ps. If the excitation signal is weaker than the vortex entry field, the disturbance of the vortex lattice is smaller than for setup 1. This can also be inferred by comparing the curves for $B_{0x} = 5$ mT in Figs. 14 and 15.

[1] M. Tinkham, *Introduction to superconductivity*. Dover Publications, Mineola/New York., Dover, 2. Edition (2004).
 [2] R. D. Parks, *Superconductivity*, (M. Dekker, New York, 1969).
 [3] P. Seidel, *Applied Superconductivity: Handbook on Devices and Applications* (Wiley-VCH Verlag, 2015).
 [4] G. R. Stewart, Superconductivity in iron compounds, *Rev. Mod. Phys.* **83**, 1589 (2011).
 [5] A. I. Buzdin, Proximity effects in superconductor-ferromagnet heterostructures, *Rev. Mod. Phys.* **77**, 935 (2005).

[6] R. Fazio and C. Lucheroni, Local density of states in superconductor-ferromagnetic hybrid systems, *Europhys. Lett.* **45**, 707 (1999).
 [7] K. Halterman and O. T. Valls, Proximity effects and characteristic lengths in ferromagnet-superconductor structures, *Phys. Rev. B* **66**, 224516 (2002).
 [8] V. N. Krivoruchko and E. A. Koshina, Inhomogeneous magnetism induced in a superconductor at a superconductor-ferromagnet interface, *Phys. Rev. B* **66**, 014521 (2002).
 [9] F. S. Bergeret, A. F. Volkov, and K. B. Efetov, Induced ferromagnetism due to superconductivity in superconductor-ferromagnet structures, *Phys. Rev. B* **69**, 174504 (2004).
 [10] R. Grein, T. Löfwander, and M. Eschrig, Inverse proximity effect and influence of disorder on triplet supercurrents in strongly spin-polarized ferromagnets, *Phys. Rev. B* **88**, 054502 (2013).
 [11] I. A. Garifullin, D. A. Tikhonov, N. N. Garif'yanov, M.Z. Fattakhov, K. Theis-Bröhl, K. Westerholt, and H. Zabel, Possible reconstruction of the ferromagnetic state under the influence of superconductivity in epitaxial V/Pd_{1-x}Fe_x bilayers, *Appl. Magn. Reson.* **22**, 439 (2002).
 [12] J. Stahn, J. Chakhalian, Ch. Niedermayer, J. Hoppler, T. Gutberlet, J. Voigt, F. Treubel, H. U. Habermeier, G. Cristiani, B. Keimer, and C. Bernhard, Magnetic proximity effect in perovskite superconductor/ferromagnet multilayers, *Phys. Rev. B* **71**, 140509(R) (2005).
 [13] J. Chakhalian, J. W. Freeland, G. Srajer, J. Stremper, G. Khaliullin, J.C. Cezar, T. Charlton, R. Dalgliesh, C. Bernhard, G. Cristiani, and H.U. Habermeier, Magnetism at the interface between ferromagnetic and superconducting oxides, *Nat. Phys.* **2**, 244 (2006).
 [14] J. Chakhalian, J. W. Freeland, H.-U. Habermeier, G. Cristiani, G. Khaliullin, M. Van Veenendaal, and B. Keimer, Orbital reconstruction and covalent bonding at an oxide interface, *Science* **318**, 1114 (2007).
 [15] J. Xia, V. Shelukhin, M. Karpovskii, A. Kapitulnik, and A. Palevski, Inverse Proximity Effect in Superconductor-Ferromagnet Bilayer Structures, *Phys. Rev. Lett.* **102**, 087004 (2009).
 [16] D. K. Satapathy, M. A. Uribe-Laverde, I. Marozau, V. K. Malik, S. Das, Th. Wagner, C. Marcelot, J. Stahn, S. Brück, A. Rühm, S. Macke, T. Tietze, E. Goering, A. Frañó, J.-H. Kim, M. Wu, E. Benckiser, B. Keimer, A. Devishvili, B. P. Toperverg, M. Merz, P. Nagel, S. Schuppler, and C. Bernhard, Magnetic Proximity Effect in YBa₂Cu₃O₇/La_{2/3}Ca_{1/3}MnO₃ and YBa₂Cu₃O₇/LaMnO_{3+δ} Superlattices, *Phys. Rev. Lett.* **108**, 197201 (2012).
 [17] M. G. Flokstra, S. J. Ray, S. J. Lister, J. Aarts, H. Luetkens, T. Prokscha, A. Suter, E. Morenzoni, and S.L. Lee, Measurement of the spatial extent of inverse proximity in a Py/Nb/Py superconducting trilayer using low-energy muon-spin rotation, *Phys. Rev. B* **89**, 054510 (2014).
 [18] J. Salafranca and S. Okamoto, Unconventional Proximity Effect and Inverse Spin-Switch Behavior in a Model Manganite-Cuprate-Manganite Trilayer System, *Phys. Rev. Lett.* **105**, 256804 (2010).
 [19] K. Rogdakis, A. Sud, M. Amado, C. M. Lee, L. McKenzie-Sell, K. R. Jeon, M. Cubukcu, M. G. Blamire, J. W. A.

- Robinson, L. F. Cohen, and H. Kurebayashi, Spin transport parameters of NbN thin films characterized by spin pumping experiments, *Phys. Rev. Mater.* **3**, 014406 (2019).
- [20] S. Kosen, R. G. E. Morris, A. F. van Loo, and A. D. Karenowska, Measurement of a magnonic crystal at millikelvin temperatures, *Appl. Phys. Lett.* **112**, 012402 (2018).
- [21] M. Vaňatka, K. Szulc, On. Wojewoda, C. Dubs, A. V. Chumak, M. Krawczyk, O. V. Dobrovolskiy, J. W. Kłos, and M. Urbánek, Spin-wave Dispersion Measurement by Variable-gap Propagating Spin-wave Spectroscopy, *Phys. Rev. Appl.* **16**, 054033 (2021).
- [22] I. A. Golovchanskiy, N. N. Abramov, V. S. Stolyarov, V. I. Chichkov, M. Silaev, I. V. Shchetinin, A. A. Golubov, V. V. Ryazanov, A. V. Ustinov, and M. Yu. Kupriyanov, Magnetization Dynamics in Proximity-coupled Superconductor-Ferromagnet-Superconductor Multilayers, *Phys. Rev. Appl.* **14**, 024086 (2020).
- [23] A. Paschoa, J. L. Gonzalez, V. P. Nascimento, and E. C. Passamani, The role of the stray field on superconducting properties of hybrid ferromagnetic/superconducting heterostructures, *J. Appl. Phys.* **128**, 043902 (2020).
- [24] A. Paschoa, J. L. Gonzalez, V. P. Nascimento, and E. C. Passamani, The role of the stray field on superconducting properties of hybrid ferromagnetic/superconducting heterostructures, *J. Appl. Phys.* **128**, 043902 (2020).
- [25] Jeon, Chiara Ciccarelli, Hidekazu Kurebayashi, Lesley F. Cohen, Sachio Komori, Jason W. A. Robinson, and Mark G. Blamire, Abrikosov vortex nucleation and its detrimental effect on superconducting spin pumping in Pt/Nb/Ni₈₀Fe₂₀/Nb/Pt proximity structures, *Phys. Rev. B* **99**, 144503 (2019).
- [26] O. V. Dobrovolskiy, R. Sachser, T. Brächer, T. Böttcher, V. Kruglyak, R. V. Vovk, V. A. Shklovskij, M. Huth, B. Hillebrands, and A. V. Chumak, Magnon-fluxon interaction in a ferromagnet/superconductor heterostructure, *Nat. Phys.* **15**, 477 (2019).
- [27] R. Cai, I. Žutić, and W. Han, Superconductor/Ferromagnet Heterostructures: A Platform for Superconducting Spintronics and Quantum Computation. *Adv. Quantum Technol.*, 2200080 (2022)..
- [28] B. Niedzielski and J. Berakdar, Controlled vortex formation at nanostructured superconductor/ferromagnetic junctions, *Phys. Status Solidi* **257**, 1900709 (2020).
- [29] B. Niedzielski, C. L. Jia, and J. Berakdar, Supercurrent induced by chiral coupling in multiferroic/superconductor nanostructures, *Nanomaterials* **11**, 184 (2021).
- [30] C. L. Jernain, S. V. Aradhya, N. D. Reynolds, R. A. Buhrman, J. T. Brangham, M. R. Page, P. C. Hammel, F. Y. Yang, and D. C. Ralph, Increased low-temperature damping in yttrium iron garnet thin films, *Phys. Rev. B* **95**, 174411 (2017).
- [31] Yunyan Yao, Qi Song, Yota Takamura, Juan Pedro Cascales, Wei Yuan, Yang Ma, Yu Yun, X. C. Xie, Jagadeesh S. Moodera, and Wei Han, Probe of spin dynamics in superconducting NbN thin films via spin pumping, *Phys. Rev. B* **97**, 224414 (2018).
- [32] Se Kwon Kim, Roberto Myers, and Yaroslav Tserkovnyak, Nonlocal Spin Transport Mediated by a Vortex Liquid in Superconductors, *Phys. Rev. Lett.* **121**, 187203 (2018).
- [33] V. V. Kruglyak, S. O. Demokritov, and D. Grundler, Magnonics, *J. Phys. D: Appl. Phys.* **43**, 264001 (2010).
- [34] A. A. Serga, A. V. Chumak, and B. Hillebrands, YIG magnonics, *J. Phys. D: Appl. Phys.* **43**, 264002 (2010).
- [35] A. V. Chumak, V. I. Vasyuchka, A. A. Serga, and B. Hillebrands, Magnon spintronics, *Nat. Phys.* **11**, 453 (2015).
- [36] A. V. Chumak, A. A. Serga, and B. Hillebrands, Magnon transistor for all-magnon data processing, *Nat. Commun.* **5**, 4700 (2014).
- [37] B. Lenk, H. Ulrichs, F. Garbs, and M. Münzenberg, The building blocks of magnonics, *Phys. Rep.* **507**, 107 (2011).
- [38] X.-g. Wang, L. Chotorlishvili, G.-h. Guo, and J. Berakdar, Electric field controlled spin waveguide phase shifter in YIG, *J. Appl. Phys.* **124**, 073903 (2018).
- [39] Q. Wang, P. Pirro, R. Verba, A. Slavin, B. Hillebrands, and A. V. Chumak, Reconfigurable nanoscale spin-wave directional coupler, *Sci. Adv.* **4**, e1701517 (2018).
- [40] Q. Wang, M. Kewenig, M. Schneider, R. Verba, F. Kohl, B. Heinz, M. Geilen, M. Mohseni, B. Lägél, F. Ciubotaru, C. Adelman, C. Dubs, S. D. Cotozana, O. V. Dobrovolskiy, T. Brächer, P. Pirro, and A. V. Chumak, A magnonic directional coupler for integrated magnonic half-adders, *Nat. Electron.* **3**, 765 (2020).
- [41] X.-g. Wang, G.-h. Guo, and J. Berakdar, Steering magnonic dynamics and permeability at exceptional points in a parity-time symmetric waveguide, *Nat. Commun.* **11**, 5663 (2020).
- [42] X.-G. Wang, G.-H. Guo, and J. Berakdar, Electric steering of spin excitation in nanostructured synthetic antiferromagnet, *Appl. Phys. Lett.* **117**, 242406 (2020).
- [43] A. Ikushima and T. Mizusaki, Superconductivity in Niobium and Niobium-Tantalum alloys, *J. Phys. Chem. Solids* **30**, 873 (1969).
- [44] L. P. Gorkov and G. M. Éliashberg, Generalization of the Ginzburg-Landau Equations for Non-Stationary Problems in the Case of Alloys with Paramagnetic Impurities. *JETP*, 27 (1968).
- [45] O. V. Dobrovolskiy, Q. Wang, D. Yu. Vodolazov, B. Budinska, R. Sachser, A. V. Chumak, M. Huth, and A. I. Buzdin, Cherenkov radiation of spin waves by ultra-fast moving magnetic flux quanta [ArXiv:2103.10156](https://arxiv.org/abs/2103.10156).
- [46] H. Kaper and J. Fleckinger-Pellé, Gauges for the Ginzburg-landau equations of superconductivity, *ZAMM - J. Appl. Math. Mech. / Z. für Angew. Math. Mechanik* **76**, 305 (1996).
- [47] G. Carneiro and E. H. Brandt, Vortex lines in films: fields and interactions, *Phys. Rev. B* **61**, 6370 (2000).
- [48] S. J. Chapman, M. D. Gunzburger, and J. S. Peterson, Simplified Ginzburg-Landau type models of superconductivity in the high kappa, high field limit, *Adv. Math. Sci. Appl.* **5**, 193 (1995).
- [49] N. Niedzielski, B. Schulz, and J. Berakdar, Spatio-temporal superconducting dynamics driven by THz fields from topological spintronic terahertz emitters, *Sci. Rep.* **12**, 15610 (2022).
- [50] V. K. Vlasko-Vlasov, A. A. Buzdin, D. Carmo, A. M. H. Andrade, A. A. M. Oliveira, W. A. Ortiz, D. Rosenmann, and W.-K. Kwok, Crossing fields in thin films of isotropic superconductors, *Phys. Rev. B* **94**, 184502 (2016).

- [51] A. A. Abrikosov, On the magnetic properties of superconductors of the second group, *Sov. Phys. JETP* **5**, 1174 (1957).
- [52] R. Engel-Herbert and T. Hesjedal, Calculation of the magnetic stray field of a uniaxial magnetic domain, *J. Appl. Phys.* **97**, 074504 (2005).
- [53] V. A. Ansteeenkiste, J. Leliaert, M. Dvornik, M. Helsen, F. Garcia-Sanchez, and B. Waeyenberge, The design and verification of MuMax3, *AIP Adv.* **4**, 107133 (2014).
- [54] D. Kumar, O. Dmytriiev, S. Ponraj, and A. Barman, Numerical calculation of spin wave dispersions in magnetic nanostructures, *J. Phys. D: Appl. Phys.* **45**, 015001 (2012).
- [55] M. Krawczyk and D. Grundler, Review and prospects of magnonic crystals and devices with reprogrammable band structure, *J. Phys.: Condens. Matter* **26**, 123202 (2014).
- [56] H. Puzkarski and M. Krawczyk, Magnonic crystals – the magnetic counterpart of photonic crystals, *Solid State Phenom.* **94**, 125 (2000).
- [57] G. Venkat, D. Kumar, M. Franchin, O. Dmytriiev, M. Mruczkiewicz, H. Fangohr, A. Barman, M. Krawczyk, and A. Prabhakar, Proposal for a standard micromagnetic problem: spin wave dispersion in a magnonic waveguide, *IEEE Trans. Magn.* **49**, 524 (2013).
- [58] F. R. Morgenthaler, An overview of electromagnetic and spin angular momentum mechanical waves in ferrite media, *Proc. IEEE* **76**, 138 (1988).
- [59] K. Y. Guslienko, B. Hillebrands, S. O. Demokritov, and A. N. Slavin, Effective dipolar boundary conditions for dynamic magnetization in thin magnetic stripes, *Phys. Rev. B* **66**, 132402 (2002).
- [60] K. Y. Guslienko, R. W. Chantrell, and A. N. Slavin, Dipolar localization of quantized spin-wave modes in thin rectangular magnetic elements, *Phys. Rev. B* **68**, 024422 (2003).
- [61] J. D. Joannopoulos, S. G. Johnson, J. N. Winn, and R. D. Meade, *Photonic Crystals: Molding the Flow of Light*, 2nd ed.; Dover Publications: **2008** (Princeton, NJ: Princeton University Press).
- [62] K.-S. Lee, D.-S. Han, and S.-K. Kim, Physical Origin and Generic Control of Magnonic Band Gaps of Dipole-exchange Spin Waves in Width-modulated Nanostrip Waveguides, *Phys. Rev. Lett.* **102**, 127202 (2009).
- [63] S.-K. Kim, K.-S. Lee, and D.-S. Han, A gigahertz-range spin-wave filter composed of width-modulated nanostrip magnonic-crystal waveguides, *Appl. Phys. Lett.* **95**, 082507 (2009).
- [64] V. N. Gladilin, J. Gutierrez, M. Timmermans, V. Vondel, J. Tempere, J. T. Devreese, and V. V. Moshchalkov, Vortices in a wedge made of a type-I superconductor, *New J. Phys.* **17**, 063032 (2015).
- [65] A. I. Gubin, K. S. Il'in, S. A. Vitusevich, M. Siegel, and N. Klein, Dependence of magnetic penetration depth on the thickness of superconducting Nb thin films, *Phys. Rev. B* **72**, 064503 (2005).
- [66] R. A. Gallardo, T. Schneider, A. Roldán-Molina, M. Langer, J. Fassbender, K. Lenz, J. Lindner, and P. Landeros, Dipolar interaction induced band gaps and flat modes in surface-modulated magnonic crystals, *Phys. Rev. B* **97**, 144405 (2018).
- [67] R. A. Gallardo, D. Cort'es-Ortuño, T. Schneider, A. Roldán-Molina, F. Ma, R. E. Troncoso, K. Lenz, H. Fangohr, J. Lindner, and P. Landeros, Flat Bands, Indirect Gaps, and Unconventional Spin-wave Behavior Induced by a Periodic Dzyaloshinskii-Moriya Interaction, *Phys. Rev. Lett.* **122**, 067204 (2019).
- [68] I. A. Golovchanskiy, N. N. Abramov, V. S. Stolyarov, V. V. Ryazanov, A. A. Golubov, and A. V. Ustinov, Modified dispersion law for spin waves coupled to a superconductor, *J. Appl. Phys.* **124**, 233903 (2018).
- [69] I. A. Golovchanskiy, N. N. Abramov, V. S. Stolyarov, V. V. Bolginov, V. V. Ryazanov, A. A. Gobulov, and A. V. Ustinov, Ferromagnet/Superconductor hybridization for magnonic applications, *Adv. Funct. Mater.* **28**, 1802375 (2018).
- [70] R. Rezaev, E. Posenitskiy, E. Smirnova, E. Levchenko, O. G. Schmidt, and V. M. Fomin, Voltage induced by superconducting vortices in open nanostructured microtubes, *Phys. Stat. Sol RRL* **13**, 1800251 (2019).
- [71] A. I. Gubin, K. S. Il'in, S. A. Vitusevich, M. Siegel, and N. Klein, Dependence of magnetic penetration depth on the thickness of superconducting Nb thin films, *Phys. Rev. B* **72**, 064503 (2005).